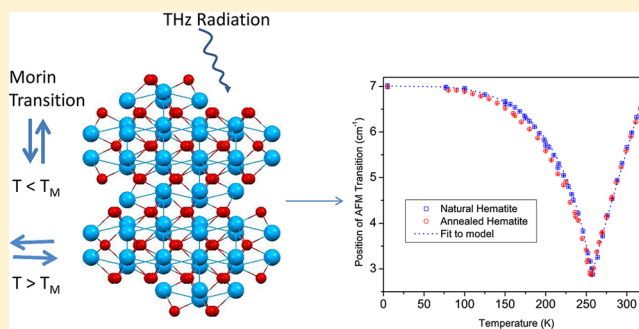


# High-Resolution Terahertz Optical Absorption Study of the Antiferromagnetic Resonance Transition in Hematite ( $\alpha\text{-Fe}_2\text{O}_3$ )

Shin G. Chou,<sup>\*,†</sup> Paul E. Stutzman,<sup>‡</sup> Shuangzhen Wang,<sup>‡</sup> Edward J. Garboczi,<sup>‡</sup> William F. Egelhoff,<sup>¶</sup> and David F. Plusquellic<sup>\*,†</sup>

<sup>†</sup>Physical Measurement Laboratory, <sup>‡</sup>Engineering Laboratory, and <sup>¶</sup>Material Measurement Laboratory, National Institute of Standards and Technology, Gaithersburg, Maryland 20899, United States

**ABSTRACT:** We report high-resolution optical absorption measurements between 1.5 and 10  $\text{cm}^{-1}$  of the antiferromagnetic (AFM) resonance transition in  $\alpha\text{-Fe}_2\text{O}_3$ . The AFM transition is measured over a range of temperatures from 4 to 325 K that includes the low- and high-temperature branches separated by a magnetic phase transition near 260 K. The high-resolution measurements devoid of optical interference were made possible by improving the frequency stability of the near-infrared lasers used to generate terahertz radiation ( $\pm 0.0003 \text{ cm}^{-1}$ ) and by taking advantage of the large temperature dependence of the AFM transition frequency. The temperature dependence of both branches could be well-fit to a magnon model. A slight difference in temperature dependence between the hematite samples with different annealing treatments was observed in the low-temperature branch. The difference is qualitatively explained by changes in the higher order crystalline anisotropy energy resulting from slightly altered magnetic interactions due to the annealing treatment. The sensitivity achieved using these methods permits a detailed characterization of the optically excited AFM magnon in the absence of magnetic fields over a wide temperature range, thus making the terahertz-based optical platform suitable for nondestructive examination applications for many AFM materials and devices.



## INTRODUCTION

Hematite ( $\alpha\text{-Fe}_2\text{O}_3$ ) is the most prevalent and thermodynamically stable phase of iron oxide.<sup>1</sup> Its exceptional chemical stability, low cost, and ease of processing make it an ideal candidate in a number of important technical applications such as sensors,<sup>2,3</sup> catalysis,<sup>4–6</sup> lithium ion batteries,<sup>7,8</sup> and solar energy production and storage.<sup>9,10</sup> The structure and properties of hematite also play an important role in the corrosion of steel in reinforced concrete in numerous parts of the national infrastructure.<sup>1</sup> While the magnetic properties of hematite do not directly impact its photoelectrochemical performance, the detailed spin configuration in hematite does have important implications on the optoelectronic and carrier transport properties of hematite-based materials and devices.

Under ambient conditions, hematite has the hexagonal corundum crystal structure.<sup>11</sup> Below the Morin transition temperature  $T_M \approx 260 \text{ K}$ , the crystal is antiferromagnetic (AFM) with the magnetic sublattices oriented antiparallel along the rhombohedral axis. Above  $T_M$  but below the Neel's transition temperature,  $T_N \approx 955 \text{ K}$ , the spins of the iron atoms flip into the basal plane and order antiferromagnetically with the moments lying in the basal plane with a slight canting away from the plane, resulting in a small net magnetization and a weakly ferromagnetic (WF) phase. The small canting of the magnetic moments results from the anisotropic exchange interaction, the Dzyaloshinski–Moriya (DM) interaction.<sup>12</sup>

The Morin transition arises from a competition of the different magnetic interactions (vide infra) within the magnetic system with different magnitudes, signs, and temperature dependencies.<sup>13</sup> At the Morin transition temperature, a change of the sign of the total free energy occurs that causes the spin flip of the AFM lattice.

The detailed structure–property relationship of hematite has been investigated using a number of methods, and its unique magnetic properties have been characterized extensively using magnetic methods.<sup>14–17</sup> On the other hand, for applications involving the examination of materials and devices, it is advantageous to make use of a noninvasive optical method to characterize the magnetic properties of such AFM materials in a zero-field configuration.

Far-infrared absorption spectroscopy has been proven to be a valuable tool for examining materials with different magnetic configurations.<sup>18–21</sup> Since the photons in the millimeter wave–terahertz region can partially penetrate most polymeric matrix materials, spectroscopic methods in this region have also been applied for imaging magnetic components in complex integrated materials and devices.<sup>18–21</sup> While far-IR absorption spectroscopic studies have been reported on several AFM

Received: April 16, 2012

Revised: July 4, 2012

Published: July 9, 2012

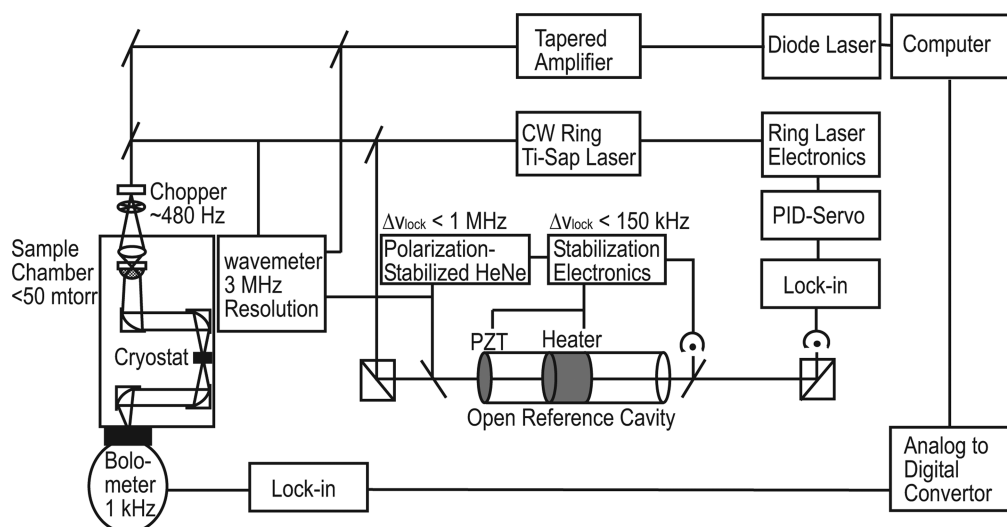


**Figure 1.** Experimental schematic of the CW high-resolution terahertz spectrometer.

materials,<sup>19,20</sup> to our knowledge, no optical characterization of the position and line width of the AFM transition in hematite has been reported. The absence of such measurements is partly due to the strong optical interference associated with high refractive index materials, as well as the lack of a broadly tunable frequency-stabilized light source in the terahertz region.<sup>19,22</sup> Unlike the electronic or phonon-assisted processes,<sup>23,24</sup> the relaxation time scale for magnetic excitations in most crystalline materials is relatively long, resulting in narrow line widths (a few gigahertz). Therefore, a high-resolution terahertz source scanning at a very small frequency step ( $\leq 10$  MHz) is required to minimize the impact of the strong interference effects and to accurately capture the peak positions and the detailed line shapes. In addition, within a temperature range relevant to most technical applications, 150–325 K, the rapid frequency shift of the AFM transition frequency with temperature that occurs near the AFM to WF phase transition makes the optical characterization of the magnetic excitation difficult.

As coherent light sources become increasingly available in the terahertz region, there has been a renewed interest to investigate and to monitor spin transitions in AFM materials, using optical methods in the terahertz region for applications in nondestructive examination (NDE). In this paper, we report the high-resolution spectroscopic characterization of the AFM transition for hematite as a function of temperature between 1.5 and  $10 \text{ cm}^{-1}$  (49–330 GHz). Since the typical resolution for most pulsed terahertz systems is limited to a few gigahertz by the travel length of the delay line, a continuous wave (CW) terahertz platform is used to achieve the spectral resolution ( $\leq 10$  MHz) required to capture the AFM transitions. The variations of the detected terahertz power from the optical interference patterns produced by the Fresnel reflections from the samples are quite extreme in this spectral region. The impact of these variations on the absorption spectra was minimized by normalizing the sample spectra against those taken at different temperatures without repositioning the sample.

## ■ EXPERIMENTAL METHODS

Several slices of hematite crystal mined in the Minas Gerais region of Brazil were used in this experiment. The samples were

cut along the (012) plane to capture both the transitions originating from spins aligned along the *c*-axis (low-temperature AFM phase) and along the basal plane (high-temperature WF phase), and the samples were characterized using X-ray diffraction method. To qualitatively understand the effects of the internal strain and defect concentration on the observed AFM transition, the samples were annealed at  $1300 \text{ }^\circ\text{C}$  for 24 h to relax the lattice and to reduce the number of defects.

The hematite samples were examined between 1.5 and  $10 \text{ cm}^{-1}$  for temperatures from 5 to 325 K using an experimental scheme similar to that previously reported<sup>25,26</sup> but with significant improvements in the frequency control of the lasers used to generate terahertz radiation. The detailed experimental scheme is shown in Figure 1.

The CW terahertz excitation energy was generated using an ErAs/GaAs photomixer.<sup>27</sup> The output from a fixed frequency single-mode ring laser near  $11\,880 \text{ cm}^{-1}$  is combined with the output from a tunable external cavity single-mode diode laser with a free-running line width  $< 500 \text{ kHz}$  and focused onto the photomixer, driving the antenna structure at the difference frequency. The resulting terahertz radiation is first collimated by a Si lens and then focused by off-axis parabolic mirrors onto the sample. The sample assembly, fixed to the coldfinger of a liquid nitrogen/liquid helium (LHe)-cooled cryostat in a sample chamber under vacuum, is placed in the terahertz beam, and the transmitted power is detected by a LHe-cooled bolometer using a 480 Hz amplitude modulation method.

Most sample scans were performed from 1.5 to  $10 \text{ cm}^{-1}$ . The precise frequency control of the lasers and the resulting sensitivity achieved are illustrated in Figure 2, where three overlapping transmission spectra are shown for consecutive scans taken 1 h apart. In many instances, the peak-to-trough signal variations are 90% of the peak power with rates of change in excess of  $50 \text{ MHz/V}$ . With such strong variations, the repeatability of the scans is essential to ensure good signal-to-noise ratios as exemplified at the top by the near-unity ratios of the three scans. To achieve this, the ring laser is actively locked to a HeNe laser stabilized transfer cavity as discussed elsewhere.<sup>28–30</sup> The frequency scan control system of the diode laser is more complex, since the scan range of  $10 \text{ cm}^{-1}$  well exceeds the fine-tuning range of the piezoelectric transducer (PZT) ( $\delta\nu \approx 2 \text{ cm}^{-1}$ ), requiring periodic grating

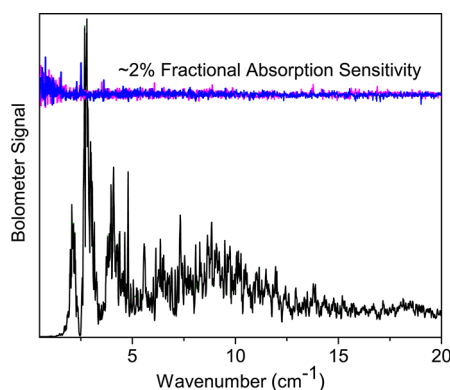


**Figure 2.** Three overlapping transmission spectra of the empty sample chamber obtained from 1.5 to 20  $\text{cm}^{-1}$  (bottom black traces) to illustrate the rapid variation of the transmitted power with increasing frequency as a result of the standing wave interference across the region. Two independent ratios of the three transmission spectra (blue and pink) are shown at the top to illustrate the repeatability of the scans.

angle adjustments for each segment of the computer-controlled PZT scan. A fast wavemeter with a relative accuracy of  $\pm 0.0003 \text{ cm}^{-1}$  was used in the interface to ensure the contiguous alignment of the PZT scans over the full scan range of the diode laser (up to 200  $\text{cm}^{-1}$ ). Data were recorded at the update rate of the wavemeter (130 Hz) and at a step resolution of 9–15 MHz. For the corresponding power variations, the rate of data acquisition was within a few time constants of the bolometer's 3 dB bandpass (450 Hz). For normalization purposes, a voltage proportional to the photomixer current is recorded simultaneously with the detected terahertz signal. After linearization, the scan accuracy was more than adequate to capture the position and line width ( $\approx 0.06 \text{ cm}^{-1}$  on average) of the AFM transition.

## RESULTS

For high refractive index materials like transition metal oxides, the acquisition of reliable absorption spectra can be challenging even with well-stabilized lasers. To illustrate this point, Figure 3 shows a comparison of the absorption spectra processed using different normalization schemes for a hematite sample at 175 K. Using a conventional approach, the transmission spectrum was normalized to the power transmitted with the sample removed (blue). In this case, a strong oscillatory background is obtained, which can be modestly improved by subtracting a sinusoidal background (red) with period characteristic of the optical thickness of the sample. A better approach to normalization is made possible in hematite because of the large frequency shift of the AFM transition with temperature throughout most of the temperature range examined from 150 to 325 K. Normalizing the transmission spectra against those taken at a slightly different temperature (black/top trace) minimizes changes in the standing wave interference patterns because of the very minor scan-to-scan differences in the sample position and dimensions. As a result, the positions and line widths of the AFM transition in the absorption spectra are nearly devoid of standing-wave artifacts. As shown in Figure 3, a clear absorption feature associated with the 175 K spectrum is measured at 6.31  $\text{cm}^{-1}$ , while the absorption feature associated with the 200 K spectrum used for normalization shows up as a well-separated negative going absorption feature at 5.75  $\text{cm}^{-1}$ .

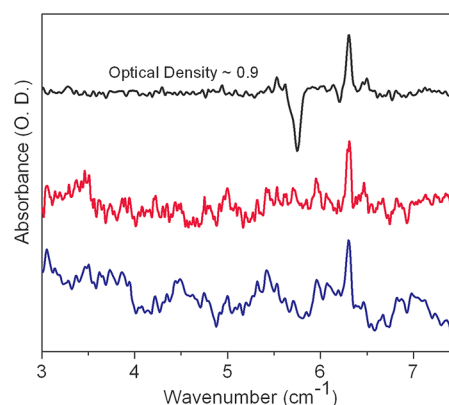


**Figure 3.** Same absorption spectrum of a 1 mm hematite sample taken at 175 K, but processed using different normalization schemes. The bottom (blue) trace shows the spectrum normalized to a empty sample cell under vacuum, where the standing-wave interference from the sample results in an oscillatory baseline. This baseline variations can be partially reduced by subtracting an artificially generated sinusoidal function, as shown in the middle (red) trace. The top (black) trace shows the same spectrum normalized to another spectrum taken at the same spot at 200 K, soon after the 175 K spectrum was obtained. Note that the baseline for each of the three traces corresponds to zero absorbance.

As the optical excitation energy is scanned between 1.5 and 10  $\text{cm}^{-1}$ , the electromagnetic wave corresponding to the AFM resonance angular frequency is absorbed, which leads to the excitation of the low-energy AFM magnon at the zone center via a magnetic dipole transition. The absorption features obtained could be fit to a single Lorentzian function with a line width in the range between 0.03 and 0.08  $\text{cm}^{-1}$ . With increasing temperature, the corresponding AFM transition changes in both the position and line width. In this report, we report on the shift in the position of the AFM magnon, while the origin of the observed line width changes will be discussed in a subsequent report.

Figure 4 shows the energies of the observed magnon frequency as a function of temperature, where each spectrum is normalized to a spectrum taken at a slightly different temperature. In each case, the temperature differential is sufficient to offset the AFM transitions from one another. The  $T_M$  for the hematite samples is estimated to be  $258 \pm 0.5 \text{ K}$ , where the lowest frequency magnon, measured at the Morin transition, was 2.88  $\text{cm}^{-1}$ . We note that the magnon frequency does not go to zero at  $T_M$ .

## DISCUSSION

As mentioned in the Introduction, the Morin transition is a magnetic phase transition arising from the competition between the different interactions in the hematite system. Specifically, the most important competing interactions include the local ionic anisotropy arising from spin–orbit coupling and the long-range dipolar anisotropy.<sup>13</sup> These interactions can have similar magnitudes and opposite signs, and their magnitudes can have different temperature dependencies. Within the context of these competing interactions, the observed temperature dependence of the magnon frequency in a temperature range near  $T_M$  is better understood within the framework of a previously reported spin wave model.<sup>31</sup> In a simplified model, where we assume the unit cell consists of a two body-centered sublattices,

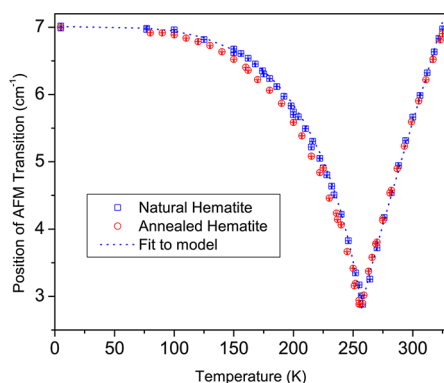


**Figure 4.** Temperature dependence of the AFM transition for the same piece of naturally occurring hematite with different annealing conditions. The data points for each sample were fitted to a spin-wave model,<sup>31</sup> but only the fit for the unannealed hematite crystal is shown. The cross through each of the hollow data point denotes the uncertainty of the measurement. The uncertainty expressed in temperature dimension is type B, with coverage factor  $k = 1$  (1 standard deviation<sup>32</sup>). The uncertainty expressed in the frequency dimension is type A, with coverage factor  $k = 1$  (1 standard deviation<sup>32</sup>).

the different energetics within the magnetic system are described by the following model Hamiltonian

$$H \approx 2J \sum_{\langle j,m \rangle} S_j \cdot S_m - B \left[ \sum_j S_{jz}^2 + \sum_m S_{mz}^2 \right] - A \sum_{\langle j,m \rangle} S_{jz} S_{mz} - D \sum_{\langle j,m \rangle} (S_j \times S_m)_z \quad (1)$$

$S_j$  and  $S_m$  are the vector spin operators associated with the  $j$ th and the  $m$ th atoms of the crystal, and the  $\sum_{\langle j,m \rangle}$  terms are extended over all nearest neighbor pairs. The first term on the right-hand side is the Heisenberg exchange interaction, which drives the spin alignment in a magnetic system. Here, the fluctuation between neighboring spins is characterized by the angle between the two spins. In the lowest energy configuration, the spins are aligned with each other. Assuming the exchange integral to be positive,  $J > 0$ , the  $j$ th and the  $m$ th spins are coupled antiferromagnetically. The second term in eq 1 denotes the one-ion, crystal-field type uniaxial anisotropy energy, and the interaction favors spin alignment along the  $\pm z$ -axis. The third term describes the dipolar type interactions associated with the precessing spins and tends to favor alignment in the  $xy$ -plane. The last term describes the Dzyloshinsky–Moriya (DM) interaction,<sup>12</sup> which is similar to the dipolar-type interaction except that the latter term tends to favor an orthogonal orientation of spins in the  $xy$ -plane. In addition to the typical magnetic interactions in antiferromagnetic systems described in eq 1, the spin wave model<sup>31</sup> also includes a contribution from a higher order crystalline anisotropy energy of the form

$$-C \left[ \sum_j S_{jz}^4 + \sum_m S_{mz}^4 \right] \quad (2)$$

While the temperature dependence measurements of the magnetic excitation provides a measure of the changing contributions of competing terms in the Hamiltonian, the limited amount of experimental information obtained in the present experiment is not sufficient to separately identify the contributions from the individual terms shown in eq 1.

Therefore, as derived in the original work, the quantized collective magnetic excitation, magnons, and their temperature dependence are captured by functions given below that describe the magnon frequency dependence on temperature. Even though most of the magnetic interactions terms were combined into simplified empirical parameters in this formulation, it is possible to obtain insight into the effect of the higher order crystalline anisotropy term when comparing different samples of hematite and the temperature dependence of their magnon frequencies.

In the low-temperature phase, the model predicts a magnon temperature dependence that is strongly modified by the inclusion of the higher order crystalline anisotropy effects, whereas the magnon energy at temperatures higher than  $T_M$  is not strongly affected by the higher order anisotropy energy.

Below  $T_M$ , the magnon energy can be written in an approximate form of

$$\hbar\omega_{L0}(T) \approx \hbar\omega_{L0}(0) [1 - (T/T_L)^4]^{1/2} \quad (3)$$

where  $T_L \approx T_M(1 + \delta)$ .  $T_L$  corresponds to the critical temperature where the magnon frequency vanishes at zone center at the phase transition.<sup>31</sup> In this form, the  $\delta$  term summarizes a number of different anisotropy interactions in the system, and the effects of high-order crystalline anisotropy strongly affect both  $\hbar\omega_{L0}(0)$  and  $\delta$ . Assuming that  $\hbar\omega_{L0}(0) \approx \hbar\omega_{L0}(S \text{ K})$ , the data are well fit to eq 3, where the effects of the higher order anisotropy are mostly captured by the  $\delta$  term.

In contrast, the magnon frequency at temperatures higher than  $T_M$  is not strongly affected by the higher order crystalline anisotropy energy. Thus, the magnon spectra collected from both the annealed and the unannealed hematite samples could be fit to a slightly altered form of eq 3, written approximately as  $\hbar\omega_{H0}(T) \approx A[-1 + (T/(T_M(1 + \Delta)))^4]^{1/2}$ .<sup>31</sup> Empirically,  $A$  and  $\Delta$  are fit to 4.09(1) and 0.46(3), and the fit is shown in Figure 4. We further note that the  $A$  and  $\Delta$  are simplified physical parameters obtained from the spin wave model.<sup>31</sup> As a result of the absence of the influence from the high-order anisotropy energy, the parameters cannot be correlated to the physical parameters shown in eq 3, despite the similar forms of the two equations.

In the low-temperature phase, even though the geometric structural information of the crystal could not be derived from the temperature dependence of the magnon spectra, the magnitude of  $\delta$  gives qualitative assessments of the changes in the higher order anisotropy of the materials without going into detailed magnetic measurements. This is illustrated by comparing hematite samples cut from the same specimen undergoing different annealing treatments. For several slices of naturally occurring hematite crystal used in this study, the fitted value of  $\delta$  is consistently found to be 0.043(1). When another slice of the same crystal was annealed to relax the lattice and to reduce defects, the inflection of the fitted curve was slightly shifted in the low-temperature branch, as shown by red circles in Figure 4. Even though the position of  $\hbar\omega_{L0}(0)$  does not change significantly,  $\delta$  is found to be 0.028(2), as shown by blue squares (fit not shown), suggesting slight alterations in higher order crystalline anisotropy as a result of the annealing treatment. (The uncertainties of the fitted parameter reported herein are type A, or 1 standard deviation.) In contrast, the temperature dependence of the magnon frequency for  $T > T_M$  does not appear to depend on the processing condition. Since the model predicts that the magnon energy at temperatures higher than  $T_M$  is not strongly affected by the inclusion of the

higher order anisotropy energy, our observations corresponds very well to the predictions of the spin wave model.

Experimentally, there has been several optical absorption studies on hematite,<sup>33–36</sup> but most optical studies to date have been focused on the spectral region between the UV and near-IR. The temperature dependence of the magnetic transitions in hematite has never been probed optically in the terahertz region. Even though the temperature dependence of magnon frequency in the lower temperature branch of hematite ( $T < T_M$ ) has been studied before, the high-temperature branch ( $T > T_M$ ) has never been measured. Overall, the optical measurements carried out here using a high-resolution terahertz platform provide an alternative method to neutron scattering<sup>37</sup> and magnetic measurements<sup>38</sup> to obtain insight into the effects of temperature on the magnetic behavior of a weak ferromagnet like hematite near a magnetic phase transition. This, in turn, provides a semiquantitative measure of the changing contributions of the competing terms in the Hamiltonian, even though the magnitude of the contribution from the individual terms could not be separately identified. The high spectral resolution data presented in this report may also provide semiquantitative means to validate some of the physical parameters derived from first-principles descriptions and methods related to ferromagnetism in antiferromagnets that have been under development.<sup>39,40</sup> However, a comprehensive comparison between the experimental findings and the different computational models available is beyond the scope of this paper.

## SUMMARY

In summary, we have conducted a series of high-resolution terahertz optical measurements of the temperature dependence of the AFM magnon transitions in hematite over a wide and technologically relevant temperature range, covering both the AFM phase below  $T_M$  and the WF phase above  $T_M$ . The temperature dependence of the magnon spectra was found to fit well with a previous developed spin wave model for hematite. A detailed comparison between the models and our data also suggests that it is possible to qualitatively assess the effect of the temperature processing condition on the magnetic interaction of the materials by a noninvasive optical means. Such information is otherwise difficult to obtain without performing detailed magnetic field dependent measurements. The data provides a semiquantitative measure of the changing contributions of the competing terms in the Hamiltonian. The results presented in this report may be used to provide a semiquantitative means to validate some of the physical parameters derived from ab initio computations. Overall, the high-resolution optical measurements as demonstrated in this study allow for the analysis of the optically excited AFM magnon, suggesting the state-resolved terahertz measurement platform could be extended for NDE applications for many AFM materials and devices whose AFM transition falls into this experimentally challenging spectral region. Furthermore, new solid state instrumentation operating with much higher power levels and scan speeds is now available in the submillimeter to terahertz regions,<sup>41</sup> which will make NDE applications utilizing instrumentations in the terahertz spectral region more widely available for practical applications. We will report in a separate publication the use of this instrumentation to achieve much higher sensitivity for detection of the AFM transitions presented herein for hematite. We expect the portability and

robust nature of this instrumentation will spur the commercial development of a new NDE platform.

## AUTHOR INFORMATION

### Corresponding Author

\*E-mail: shinchou@alum.mit.edu (S.G.C.); dplus@nist.gov (D.F.P.).

### Notes

The authors declare no competing financial interest.

## ACKNOWLEDGMENTS

The authors acknowledge the foresight of Dr. W. F. Egelhoff and Dr. K. Gilmore, whose scientific vision has led to the conception of this project. The authors gratefully acknowledge J. Surek for procuring one of the hematite samples used in this study. Two of the authors (S.G.C. and D.F.P.) gratefully acknowledge useful discussions with Dr. R. McMichael, Dr. N. Martys, and Dr. E. Shirley. S.W. acknowledges support from the ARRA Fellowship. The work was supported by the NIST Innovative Measurement Science research program. Certain equipment or materials are identified in this paper in order to specify the experimental procedure adequately. Such identification is not intended to imply endorsement by the National Institute of Standards and Technology, nor is it intended to imply that the materials or equipment identified are necessarily the best available.

## REFERENCES

- (1) Cornell, R. M.; Schwertmann, U. *The Iron Oxides, Structure, Properties, Reactions, Occurrences, and Uses*; Wiley-VCH: New York, 2003.
- (2) Choi, W. S.; Koo, H. Y.; Zhongbin, Z.; Li, Y.; Kim, D.-Y. *Adv. Funct. Mater.* **2007**, *17*, 1743–1749.
- (3) Gou, X.; Wang, G.; Park, J.; Liu, H.; Yang, J. *Nanotechnology* **2008**, *19*, 125606.
- (4) Herrera, F.; Lopez, A.; Mascolo, G.; Albers, E.; Kiwi, J. *Appl. Catal., B* **2001**, *29*, 147–162.
- (5) Huang, H.; Lu, M.; Chen, J. *Water Res.* **2001**, *35*, 2291–2299.
- (6) Shekhah, O.; Ranke, W.; Schule, A.; Kolios, G.; Schlogl, R. *Angew. Chem., Int. Ed.* **2003**, *42*, 5760–5763.
- (7) Zeng, S.; Tang, K.; Li, T.; Liang, Z.; Wang, D.; Wang, Y.; Zhou, W. *J. Phys. Chem. C* **2007**, *111*, 10217–10225.
- (8) Wu, Z.; Yu, K.; Zhang, S.; Xie, Y. *J. Phys. Chem. C* **2008**, *112*, 11307–11313.
- (9) Sivula, K.; Zboril, R.; Le Formal, F.; Robert, R.; Weidenkaff, A.; Tucek, J.; Frydrych, J.; Graetzel, M. *J. Am. Chem. Soc.* **2010**, *132*, 7436–7444.
- (10) Tran, P. D.; Wong, L. H.; Barber, J.; Loo, J. S. C. *Energy Environ. Sci.* **2012**, *5*, 5902–5918.
- (11) Pauling, L.; Hendricks, S. *J. Am. Chem. Soc.* **1925**, *47*, 781–790.
- (12) Dzyaloshinsky, I. *J. Phys. Chem. Solids* **1958**, *4*, 241–255.
- (13) Artman, J.; Murphy, J.; Foner, S. *Phys. Rev.* **1965**, *138*, A912.
- (14) Moriya, T. *Magnetism I*; Academic Press: New York, 1963; Chapter 3 and references cited in this article.
- (15) Morrish, A. H. *Canted Antiferromagnetism*; World Scientific: River Edge, NJ, 1994.
- (16) Foner, S.; Williamson, S. J. *J. Appl. Phys.* **1965**, *36*, 1154.
- (17) Jacobs, I. S.; Beyerlein, R. A.; Foner, S.; Remeika, J. P. *Int. J. Magnet.* **1971**, *1*, 193–208.
- (18) Aguilar, R. V.; Sushkov, A. B.; Park, S.; Cheong, S. W.; Drew, H. D. *Phys. Rev. B* **2006**, *74*.
- (19) Ohlmann, R. C.; Tinkham, M. *Phys. Rev.* **1961**, *123*, 425–434.
- (20) Sievers, A. J.; Tinkham, M. *Phys. Rev.* **1963**, *129*, 1566–1571.
- (21) Quijada, M. A.; Simpson, J. R.; Vasiliu-Doloc, L.; Lynn, J. W.; Drew, H. D.; Mukovskii, Y. M.; Karabashev, S. G. *Phys. Rev. B* **2001**, *64*, 224426.

- (22) Roberts, S.; Jacobs, I. S. *AIP Conf. Proceed.* **1973**, *10*, 107–111.
- (23) Basov, D.; Averitt, R.; van der Marel, D.; Dressel, M.; Haule, K. *Rev. Mod. Phys.* **2011**, *85*, 471.
- (24) Chou, S.; DeCamp, M.; Jiang, J.; Samsonidze, G.; Barros, E.; Plentz, F.; Jorio, A.; Zheng, M.; Onoa, G.; Semke, E.; Tokmakoff, A.; Saito, R.; Dresselhaus, G.; Dresselhaus, M. *Phys. Rev. B* **2005**, *72*, 195415.
- (25) Ahmed, Z.; Chou, S. G.; Siegrist, K.; Plusquellic, D. F. *Faraday Discuss.* **2011**, *150*, 175–192.
- (26) Siegrist, K.; Bucher, C. R.; Mandelbaum, I.; Hight Walker, A. R.; Balu, R.; Gregurick, S. K.; Plusquellic, D. F. *J. Am. Chem. Soc.* **2006**, *128*, 5764–5775.
- (27) Brown, E.; Mcintosh, K.; Nichols, K.; Dennis, C. *Appl. Phys. Lett.* **1995**, *66*, 285–287.
- (28) Niebauer, T. M.; Faller, J. E.; Godwin, H. M.; Hall, J. L.; Barger, R. L. *Appl. Opt.* **1988**, *27*, 1285–1289.
- (29) Riedle, E.; Ashworth, S. H.; Farrell, J. T.; Nesbitt, D. J. *Rev. Sci. Instrum.* **1994**, *65*, 42–48.
- (30) Podobedov, V.; Plusquellic, D.; Fraser, G. J. *Quant. Spectrosc. Radiat. Transfer* **2005**, *91*, 287–295.
- (31) Nagai, O.; Bonavito, N. L.; Tanaka, T. *J. Phys. C: Solid State Phys.* **1975**, *8*, 176.
- (32) Taylor, B. N.; Kuyatt, C. E. *NIST Tech. Note* **1994**, 1297.
- (33) Marusak, L.; Messier, R.; White, W. J. *Phys. Chem. Solids* **1980**, *41*, 981–984.
- (34) Balberg, I.; Pinch, H. J. *Magn. Magn. Mater.* **1978**, *7*, 12–15.
- (35) Chen, C.; Cahan, B. J. *Opt. Soc. Am.* **1981**, *71*, 932–934.
- (36) Galuza, A.; Beznosov, A.; Eremenko, V. *Low Temp. Phys.* **1998**, *24*, 726–729.
- (37) Hill, A. H.; Jiao, F.; Bruce, P. G.; Harrison, A.; Kockelmann, W.; Ritter, C. *Chem. Mater.* **2008**, *20*, 4891–4899.
- (38) Kvardakov, V.; Sandonis, J.; Podurets, K.; Shilstein, S.; Barushel, J. *Physica B* **1991**, *168*, 242–250.
- (39) Mazurenko, V.; Anisimov, V. *Phys. Rev. B* **2005**, *71*.
- (40) Sandratskii, L.; Kubler, J. *Europhys. Lett.* **1996**, *33*, 447–452.
- (41) Gerecht, E.; Douglass, K. O.; Plusquellic, D. F. *Opt. Express* **2011**, *19*, 8973–8984.